



Interplanetary Sheaths and Corotating Interaction Regions: A Comparative Statistical Study on Their Characteristics and Geoeffectiveness

Rajkumar Hajra¹ · Jibin V. Sunny¹ · Megha Babu² · Archana Giri Nair²

Received: 7 April 2022 / Accepted: 8 June 2022
© The Author(s), under exclusive licence to Springer Nature B.V. 2022

Abstract

Interplanetary sheaths and corotating interaction regions (CIRs), while having different solar sources, represent turbulent solar-wind plasma and magnetic field that can perturb the Earth's magnetosphere. We explore long-term solar-wind measurements upstream of the Earth during Solar Cycle 24, from January 2008 to December 2019, to compare their solar-cycle variation, characteristic features, and geoeffectiveness. Earth is found to be encountered by ≈ 2.6 times more CIRs (290) than sheaths (110) during this period. The sheath occurrence follows the $F_{10.7}$ solar radio-flux variation, with a cross-correlation coefficient (r_{cc}) of +0.71 at zero-year time lag. However, the CIR occurrence is more prominent during the solar cycle descending to minimum phases, reflected in r_{cc} values of -0.53 and $+0.50$ at time lags of -2 and $+4$ years, respectively, between the CIR occurrence and the $F_{10.7}$ solar flux. Both sheath and CIR are characterized by identical average plasma density and interplanetary magnetic-field (IMF) magnitude, and their fluctuations characterized by enhanced variance, and periodic variations of a few minutes to an hour. However, on average, the CIR has $\approx 12\%$ higher plasma speed, $\approx 33\%$ higher temperature, $\approx 20\%$ stronger southward IMF component, $\approx 131\%$ longer duration, and $\approx 158\%$ longer radial extent than the sheath. The intensities of the auroral electrojet index [AE] and the symmetric ring-current index [SYM-H] are, respectively, $\approx 38\%$ and $\approx 55\%$ stronger during the CIR than the sheath, on average. The geoeffectiveness of the CIR is found to be significantly higher than the sheath. Among all CIRs (sheaths), $\approx 25\%$ ($\approx 14\%$) caused moderate storms ($-50 \text{ nT} \geq \text{SYM-H} > -100 \text{ nT}$), and $\approx 5\%$ ($\approx 4\%$) caused intense storms ($\text{SYM-H} \leq -100 \text{ nT}$).

✉ R. Hajra
raj कुमारhajra@yahoo.co.in

J.V. Sunny
jibinvsunny@gmail.com

M. Babu
meghabnair1999@gmail.com

A.G. Nair
archanagnair1998@gmail.com

¹ Indian Institute of Technology Indore, Simrol, Indore, Madhya Pradesh 453552, India

² Department of Sciences, Amrita School of Engineering, Amrita Vishwa Vidyapeetham, Amritanagar, Coimbatore, Tamil Nadu 641112, India

Keywords Coronal holes · Coronal mass ejections, interplanetary · Magnetic fields, interplanetary · Magnetosphere, geomagnetic disturbances · Solar cycle, observations · Solar wind

1. Introduction

Space weather is a broad topic of interest for modern society that is increasingly dependent on various forms of space-technology systems (see Echer et al., 2005; Cannon et al., 2013; Hajra, Tsurutani, and Lakhina, 2020; Lakhina, Hajra, and Tsurutani, 2020, and references therein). Interplanetary sheaths and corotating interaction regions (CIRs) are among the most important space-weather events that can potentially impact such systems. They represent compressed, turbulent, heated plasma, and interplanetary magnetic fields (IMFs), which are known to cause geomagnetic disturbances. While both of them initiate on the Sun, their solar sources are different. A coronal mass ejection (CME) erupted from the active region on the Sun and propagating fast in the interplanetary medium, that is interplanetary CME (ICME), is preceded by a piled-up solar wind or the interplanetary sheath (Kennel, Edmiston, and Hada, 1985; Tsurutani and Lin, 1985; Tsurutani et al., 1988). A fast-forward shock can form at the sheath leading edge when the ICME speed exceeds the ambient solar-wind speed by the local magnetosonic wave speed (Landau and Lifshitz, 1960; Kennel, Edmiston, and Hada, 1985; Tsurutani et al., 2011). On the other hand, a CIR forms when a coronal hole emanated high-speed stream (HSS) interacts with the ambient slow stream (Davis, 1966; Davis et al., 1966; Belcher and Davis, 1971; Burlaga, 1974; Smith and Wolfe, 1976; Gosling et al., 1978; Pizzo, 1985). A pair of fast-forward and fast-reverse shocks can form at the CIR leading and trailing edges, respectively, beyond ≈ 2 AU from the Sun (Gosling, Hundhausen, and Bame, 1976; Smith and Wolfe, 1976; Hajra, 2021a).

Enhanced plasma speed, ram pressure, and most importantly southward IMF components during the sheaths and CIRs, are responsible for their significant impacts on the inner magnetospheric ring current (Tsurutani et al., 1988, 1995; Huttunen, Koskinen, and Schwenn, 2002; Huttunen and Koskinen, 2004; Tsurutani et al., 2006; Alves, Echer, and Gonzalez, 2006; Echer et al., 2008; Chi et al., 2018), radiation-belt relativistic electrons (Hajra et al., 2014, 2015a,b; Hajra, Tsurutani, and Lakhina, 2020; Tsurutani et al., 2016a,b; Hajra and Tsurutani, 2018; Hajra, 2021b), auroral ionosphere (Tsurutani and Gonzalez, 1987; Hajra et al., 2013, 2017; Kilpua et al., 2013; Kilpua, Koskinen, and Pulkkinen, 2017), and atmosphere (Lei et al., 2011; Gardner et al., 2012). While there are apparent similarities between the two types of space-weather events, there are significant differences in their solar sources, solar-cycle variations, and impacts. As mentioned above, sheaths are associated with CMEs erupted from the active regions on the Sun, while CIRs are associated with HSSs emanated from the solar coronal holes. This leads to their varying solar-cycle variations. In addition, a major fraction of the strongest storms is known to be caused by the sheaths (Tsurutani et al., 1988; Huttunen, Koskinen, and Schwenn, 2002; Huttunen and Koskinen, 2004; Echer et al., 2008), while CIRs are known to be responsible for a major fraction of the moderate storms at the Earth (Alves, Echer, and Gonzalez, 2006; Chi et al., 2018; Hajra and Sunny, 2022).

While both sheaths and CIRs are well-explored topics, there is no significant comparative study between the events. The aim of this work is to conduct a detailed comparison of their solar-cycle variations, solar-wind and IMF characteristic features, and the impacts on the magnetosphere–ionosphere system. The study is performed using a long database covering a full solar cycle to ensure the robustness of the statistical results. Such a study is important for augmentation of characterization and predictability of space-weather events and their impacts.

2. Data and Methods

2.1. Data Sources

High-resolution (one-minute) solar-wind plasma and IMF data analyzed in this work are taken from NASA's OMNIWeb (omniweb.gsfc.nasa.gov/). The plasma is characterized by plasma speed [V_{sw}], density [N_{sw}], ram pressure [P_{sw}], temperature [T_{sw}], and plasma- β (the ratio of the plasma pressure to the magnetic pressure). The IMF measurements, namely the IMF magnitude [B_0], and the B_x -, B_y -, and B_z -components, are in the geocentric solar magnetospheric (GSM) coordinate system. The plasma and IMF data are used to identify and characterize the solar-wind and interplanetary features of interplanetary sheaths and CIRs.

To verify the solar sources of sheaths and CIRs, we explored the CME catalog available at the *Coordinated Data Analysis Workshops* (CDAW: cdaw.gsfc.nasa.gov/), and the coronal hole images available at the *Solar Dynamics Observatory* (SDO: sdo.gsfc.nasa.gov/), respectively.

The geomagnetic activity associated with sheaths and CIRs are studied using geomagnetic indices, namely the horizontal component of the symmetric ring-current index [SYM-H] (Dessler and Parker, 1959; Wanliss and Showalter, 2006; Iyemori et al., 2010), and the auroral electrojet index [AE] (Rostoker, 1972). High-resolution (one-minute) geomagnetic indices are obtained from the *World Data Center for Geomagnetism*, Kyoto, Japan (WDC: wdc.kugi.kyoto-u.ac.jp/).

The $F_{10.7}$ solar radio fluxes are used to study the ≈ 11 -year solar-cycle (Schwabe, 1844) variation. The yearly fluxes are obtained from the *Laboratory for Atmospheric and Space Physics Interactive Solar Irradiance Data Center* (lasp.colorado.edu/lisird/).

2.2. Methods

As mentioned above, an interplanetary sheath is a piled-up, compressed solar wind ahead of an ICME. When the driving ICME speed exceeds the ambient speed by the local magnetosonic speed, a fast-forward shock (FS) can form at the sheath leading edge. While sheaths can be observed without a leading fast shock (for slow ICMEs), to avoid any ambiguity we only considered sheaths that are preceded by shocks and followed by prominent ICME signatures, like enhanced IMF B_0 , and smooth rotation(s) in the IMF component(s) (see Zurbuchen and Richardson, 2006, and references therein).

Sheaths are identified from the temporal variation of the solar-wind parameters as follows. First, an interplanetary fast FS is identified by an abrupt increase in V_{sw} with simultaneous increases in N_{sw} , T_{sw} , and B_0 . Secondly, to confirm the CME eruption as the solar source of the identified shock, the CDAW CME catalog is explored. Thirdly, prominent ICME signatures are verified by low T_{sw} , plasma- β , and/or smooth rotation(s) in the IMF component(s). Finally, the region between a fast FS and an ICME with compressed plasma and magnetic field is identified as a sheath. Following this method, we identified a total of 110 sheaths from January 2008 through December 2019. These are listed in Table 3 in the Appendix.

The CIR events studied in this work are taken from Hajra and Sunny (2022), which we refer the reader to for a detailed description of the CIR identification method. In brief, a CIR is identified as the region of the compressed (high) N_{sw} and IMF B_0 between a slow stream and an HSS emanated from a solar coronal hole (Smith and Wolfe, 1976). The number of CIRs analyzed in this work is 290, between January 2008 and December 2019.

The compressed and turbulent sheaths and CIRs are characterized by the average V_{sw} [$<V_{sw}>$], the peak values of N_{sw} , P_{sw} , T_{sw} , and B_0 , and the minimum B_z during their intervals. We also estimated their duration from the start to the end of the events. The characteristic radial extent of the dynamic events is computed as the “area under the V_{sw} curve”.

Sheaths and CIRs are defined to be geoeffective when the peak (minimum) SYM-H index during their intervals is less than -50 nT. According to Gonzalez et al. (1994), a SYM-H peak between -50 and -100 nT defines a moderate storm, and a SYM-H peak below -100 nT defines an intense storm.

To quantify the fluctuating/periodic variations of IMF during sheaths and CIRs, variance analysis is performed. The one-minute resolution IMF components are used to construct the field variances (σ_x^2 , σ_y^2 , σ_z^2) at three time intervals, 5, 15, and 45 minutes, and make 45-minute averages of the variances. The shorter-interval variances are “nested” inside the longer-interval variances. A high variance value indicates a large amount of wave power for frequencies up to the variance time value, while a low variance implies reduced wave power in that frequency range (Tsurutani et al., 1982; Hajra et al., 2013, 2017; Hajra and Tsurutani, 2022). Thus, the combined variances can be considered as a low-resolution power spectrum.

We performed a continuous wavelet analysis in order to study the temporal variation of the prominent periodicity in the solar-wind variations. The wavelet transform is a suitable technique to analyze a nonstationary time series. For the present work, we used the Morlet wavelet (see Torrence and Compo, 1998; Hajra et al., 2021, and references therein).

We also apply the Lomb–Scargle periodogram analysis (Lomb, 1976; Scargle, 1982) to identify the significant periodicities in specific solar-wind intervals. It is a useful tool for detecting and characterizing periodic signals for unevenly spaced data (e.g., Marques de Souza Franco et al., 2021, and references therein).

To study the relationship of the sheath and CIR occurrences with the $F_{10.7}$ solar fluxes, we use the classical cross-correlation analysis (Davis, 2002). The cross-correlation between two time series is computed by displacing one time series relative to the other in time. Thus, the successive lags and correlation coefficients, and the lag corresponding to the maximum correlation between the two series can be obtained.

We estimated the statistical probability factor or the two-tailed p -value (Reiff, 1990) based on the mean values and standard deviations of the sheath and CIR characteristic parameters and geomagnetic indices during them. A p -value less than 0.05 ($p < 0.05$) indicates that the two means are significantly different (Press et al., 1992).

3. Results and Discussion

3.1. Case Studies

Figure 1 shows solar-wind variations and geomagnetic impacts of a CIR occurring during days 68–69 of 2008, and an interplanetary sheath during days 215–216 of 2010. The top panels, from Figure 1(a) to Figure 1(l), depict the solar-wind and interplanetary conditions. The bottom panels, from Figure 1(m) to Figure 1(p), show the geomagnetic conditions.

The CIR (Figure 1, left panel) is formed between a slow solar wind with $V_{sw} \approx 325 \text{ km s}^{-1}$ on days 67–68 and an HSS with a peak $V_{sw} \approx 738 \text{ km s}^{-1}$ on day 71 of 2008. The solar source of the HSS is a large, positive-polarity coronal hole (marked by number 50), prominently visible from the equator to the southern hemisphere of the Sun on days 68–69 (not shown). The CIR interval extended from ≈ 0656 UT on day 68 to ≈ 1254 UT on day 69 (marked by a blue shaded interval in Figure 1, left panel). While there

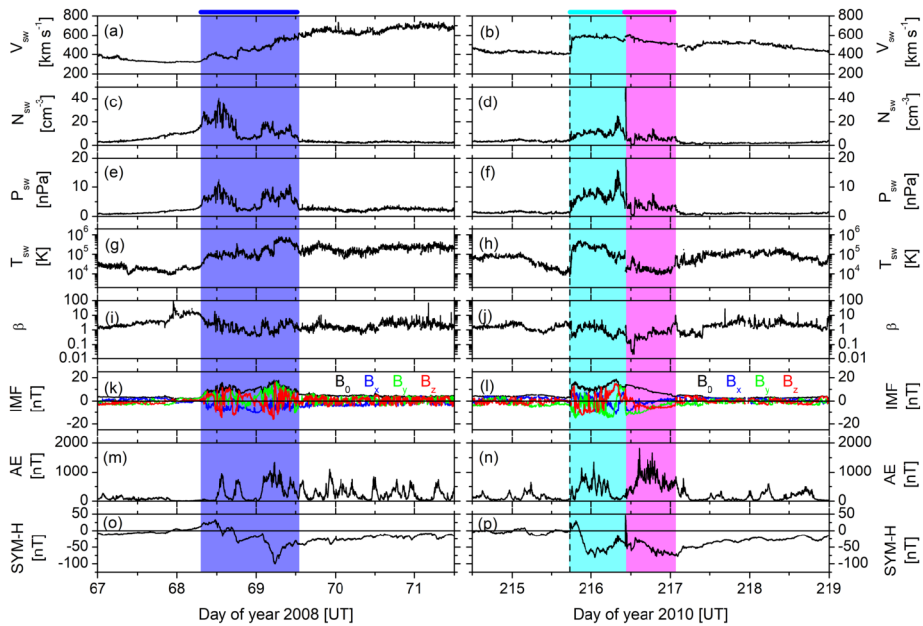


Figure 1 Solar-wind variations and geomagnetic effects during days 67–71 of 2008 (*left*) and days 214–218 of 2010 (*right*). From top to bottom, the panels show (a–b) solar-wind plasma speed [V_{sw}], (c–d) plasma density [N_{sw}], (e–f) ram pressure [P_{sw}], (g–h) temperature [T_{sw}], (i–j) plasma- β , (k–l) IMF magnitude [B_0], and B_x -, B_y -, and B_z -components, and geomagnetic indices (m–n) AE, and (o–p) SYM-H. The shaded regions and horizontal bars at the top show a CIR (*blue*), a sheath (*light cyan*), and an MC (*light magenta*). The vertical dashed line in the *right panel* shows an interplanetary fast-forward shock.

is no sharp boundary of the CIR (in the solar-wind data), it is identified by gradually increasing B_0 peaking to ≈ 18 nT at 0521 UT on day 69, followed by its gradual decrease. While the IMF components are highly fluctuating during the HSS proper, the fluctuation amplitude is significantly enhanced during the CIR interval. N_{sw} and P_{sw} are also compressed, with peak values of ≈ 41 cm $^{-3}$ and ≈ 13 nPa, respectively, during the CIR event.

Magnetospheric compression by the P_{sw} enhancement at the CIR leading edge is associated with a gradual increase in SYM-H to 32 nT (Figure 1(o)). This was followed by two episodes of southward IMF with the minimum $B_z \approx -15$ nT and ≈ -13 nT and duration of ≈ 1.78 hours and ≈ 1.77 hours, respectively. These are correlated with AE increases with maximum AE values of 941 nT and 737 nT, and minimum SYM-H values of -17 nT and -38 nT, respectively. A stronger (B_z minimum = -16 nT) and longer-duration (≈ 2.48 hours) IMF southward component led to a stronger SYM-H negative excursion to -100 nT at ≈ 0540 UT on day 69. This was associated with an AE increase to 1341 nT. Thus, the CIR is found to be geoeffective causing an intense magnetic storm with a three-step main-phase development.

The interplanetary structures during days 214–217 of 2010 (Figure 1, right panel) are associated with a halo CME that erupted at a speed of 850 km s $^{-1}$ from the Sun at ≈ 1342 UT on day 213 (not shown). The interplanetary counterpart of the CME (i.e., ICME), moving faster than the ambient solar wind, caused a fast FS at ≈ 1743 UT on day 215 (marked by a vertical dashed line). The FS can be identified by sharp and simultaneous increases in V_{sw} from ≈ 409 to 585 km s $^{-1}$, in N_{sw} from ≈ 3.6 to 11.9 cm $^{-3}$, in P_{sw} from ≈ 1.5 to 5.4 nPa,

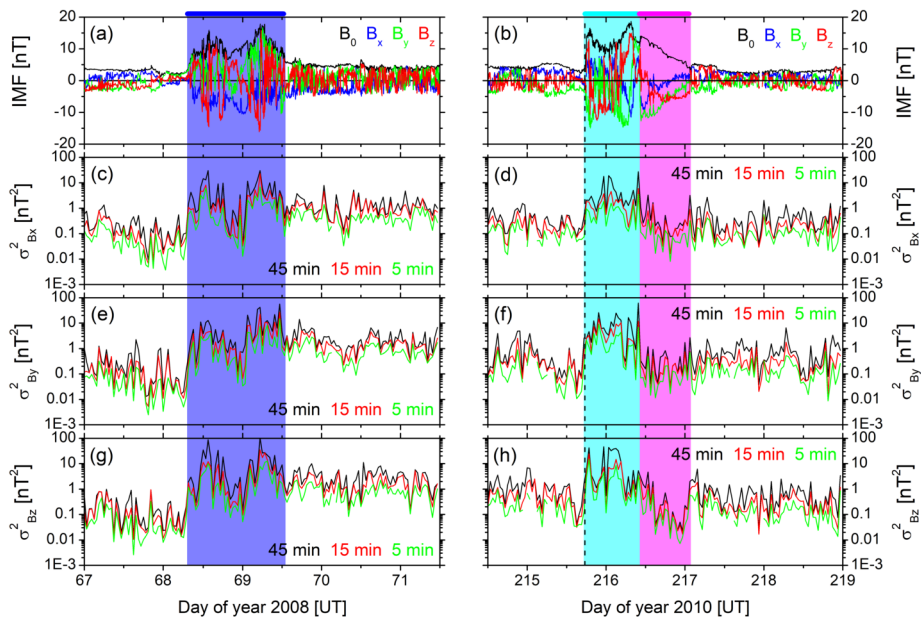


Figure 2 Variations of IMF during days 67–71 of 2008 (left) and days 214–218 of 2010 (right). From top to bottom, panels are (a–b) IMF B_0 (black) and B_x - (blue), B_y - (green), and B_z - (red) components, variances in (c–d) B_x , (e–f) B_y , and (g–h) B_z . Markings of interplanetary structures are repeated from Figure 1 for reference.

in T_{sw} from $\approx 1.0 \times 10^4$ to 1.6×10^5 K, and in IMF B_0 from ≈ 3.3 to 14.0 nT. This caused a sudden impulse (SI⁺) of +23 nT in SYM-H (Figure 1(p)).

The FS is followed by a sheath up to ≈ 1038 UT on day 216. This is characterized by strong fluctuations in the IMF components, and enhancements in B_0 (≈ 18.7 nT), V_{sw} (≈ 604 km s⁻¹), N_{sw} (≈ 24.9 cm⁻³), P_{sw} (≈ 15.7 nPa), and T_{sw} ($\approx 5 \times 10^5$ K). IMF B_z shows a long-duration southward component with a peak value of -12.6 nT. This led to a moderate magnetic storm with the SYM-H minimum of -81 nT at ≈ 0110 UT on day 216.

Following the sheath, the IMF components show smooth rotations up to ≈ 0122 UT on day 217. This interval is characterized by a minimum $T_{sw} \approx 1.0 \times 10^4$ K and a minimum β of 0.02. This represents a flux-rope magnetic cloud (MC: Burlaga et al., 1981; Klein and Burlaga, 1982; Tsurutani and Gonzalez, 1997). However, a detailed study of the MC is beyond the scope of the present work.

The most prominent and common feature of the sheath and CIR shown in Figure 1 is the presence of fluctuations in the IMF components. Kilpua et al. (2013) investigated ultralow-frequency (ULF) IMF and P_{sw} fluctuations (with corresponding periods of 3–10 minutes) for 41 sheaths during Solar Cycle 23. Moissard, Fontaine, and Savoini (2019) identified high levels of turbulent energy in the IMF fluctuations during 42 sheaths between 1998 and 2006.

To study the IMF fluctuations during the CIR and the sheath, we estimated the IMF-component variances (Figure 2) during the events shown in Figure 1. With the commencement of the CIR (Figure 2, left panel), variances increase in all IMF-components compared to their values before the CIR impact. While IMF B_0 is significantly higher during the CIR compared to that during the following HSS interval, variances during the HSS interval are comparable to those during the CIR. High IMF variances during the CIR/HSS are associated with Alfvén-wave activity.

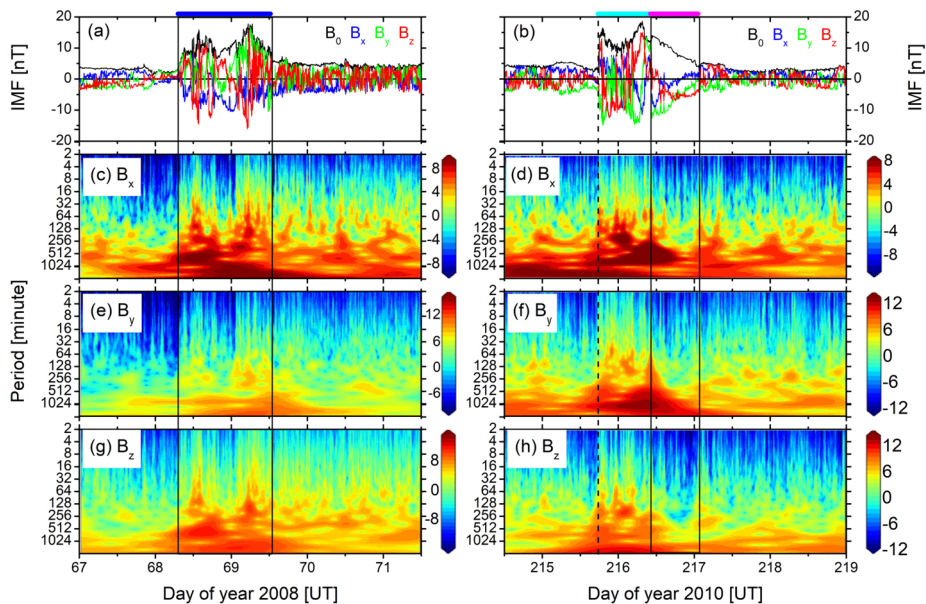


Figure 3 Wavelet analysis of IMF during days 67–71 of 2008 (left) and days 214–218 of 2010 (right). From top to bottom, panels are (a–b) IMF B_0 (black) and B_x - (blue), B_y - (green), and B_z - (red) components, wavelet spectrum of (c–d) B_x , (e–f) B_y , and (g–h) B_z . The color bars on the right of each wavelet spectrum indicate the wavelet spectral power of the observed periods in arbitrary units. Horizontal bars at the top indicate a CIR (blue), a sheath (cyan), and an MC (magenta). An interplanetary shock is shown by a vertical dashed line.

The IMF variances during the sheath (Figure 2, right panel) are almost identical to those during the CIR. The variances clearly increase during the sheath in comparison to those before the shock commencement. Interestingly, variances decrease during the MC, that is characterized by smooth rotations in the IMF components.

Figure 3 shows the continuous Morlet wavelets of the IMF components. Compared to the pre-CIR interval (Figure 3, left panel), smaller-period (higher-frequency) fluctuations are found to be enhanced in amplitude during the CIR and HSS intervals. This is most prominent in the B_z -component (Figure 3(g)), where strong power can be noted from ≈ 15 minutes to a few hours. Enhanced power of the lower-period fluctuations during the sheath is followed by disappearance of the same during the following MC interval (Figure 3, right panel).

The above results are further confirmed by the Lomb–Scargle periodogram analysis shown in Figure 4. For this, 4-hour intervals are selected before the CIR (marked as low-speed stream or LSS), during the CIR, during the HSS, before the sheath impact, during the sheath, and during the MC. These are marked by color-coded bars at the top of Figure 4. Both during the CIR (Figure 4(e)) and the sheath (Figure 4(f)), 30-minutes to 1-hour periods have statistically significant power (above the 95% confidence level). This result again confirms high-frequency fluctuations or the turbulent nature of CIR and sheath.

3.2. Solar-Cycle Variations

Figure 5(a) shows the solar-cycle variations of all sheaths (110) and CIRs (290) under this study. The yearly occurrences are computed from the total number of events in each year

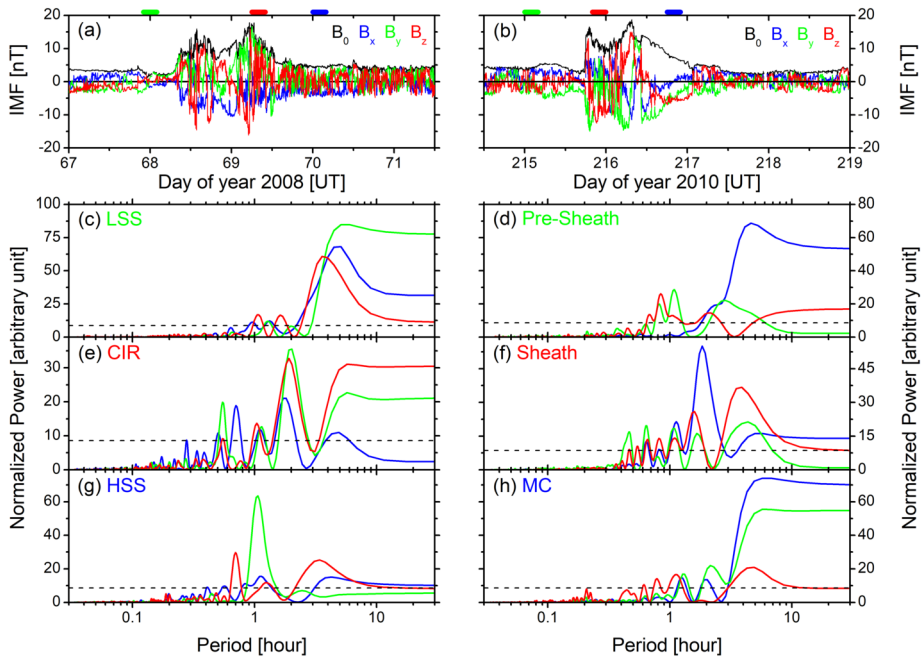


Figure 4 Lomb–Scargle periodograms of IMF during days 67–71 of 2008 (*left*) and days 214–218 of 2010 (*right*). From top to bottom, panels are (a–b) IMF B_0 (black) and B_x - (blue), B_y - (green), and B_z - (red) components, periodograms of the IMF components during (c) low-speed stream (LSS), (d) interval before sheath, (e) CIR, (f) sheath, (g) HSS, and (h) MC. Durations of the periodograms are shown by color-coded bars in the top panel. The 95% confidence level of the periodograms is shown by the horizontal dashed lines.

as a percentage of the total number during the entire period of observation. As shown by the yearly mean $F_{10.7}$ solar-flux variation, solar activity is significantly higher during the years 2012 to 2015, with the maximum yearly mean flux in 2014. The sheath occurrence follows the $F_{10.7}$ variation, attaining a peak in 2012. It can be noted that, when considering the monthly mean $F_{10.7}$ solar flux, Solar Cycle 24 has two peaks: one peak during November 2011, and another one during February 2014 (not shown). Thus, the 2012 sheath peak seems to be associated with the first solar-activity peak. The association of the sheath occurrence with the $F_{10.7}$ variation is confirmed by a high cross-correlation coefficient (r_{cc}) of +0.71 at 0-year time lag between the two (Figure 5(b)). The sheath solar-cycle variation is found to be consistent with the solar-cycle variation of the driving ICMEs (see Richardson and Cane, 2012; Wu and Lepping, 2016; Kilpua, Koskinen, and Pulkkinen, 2017, and references therein).

On the other hand, the CIR occurrence is much more uniformly distributed through the solar cycle, with slightly higher occurrence during the descending to minimum phases of the solar cycle (Figure 5(a)). This solar-cycle variation pattern is reflected in a significant cross-correlation coefficient of the CIR occurrence at -2 -year ($r_{cc} = -0.53$) and $+4$ -year ($r_{cc} = +0.50$) time lags with the $F_{10.7}$ solar flux. The CIR solar-cycle variation is consistent with previous results (e.g., Alves, Echer, and Gonzalez, 2006; Jian et al., 2006, 2019; Hajra and Sunny, 2022).

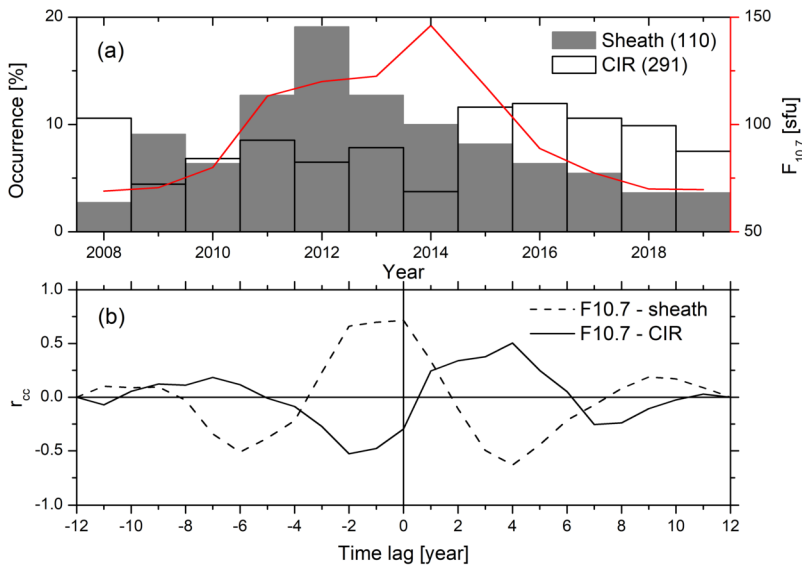


Figure 5 (a) Yearly occurrences (scale on the left) of sheaths (gray histogram) and CIRs (empty histogram), and yearly mean $F_{10.7}$ solar flux (red, scale on the right). (b) Cross-correlations (r_{cc}) of yearly occurrences of sheaths and CIRs with yearly mean $F_{10.7}$ solar flux. The $F_{10.7}$ is given in solar flux unit (sfu), where 1 sfu = $10^{-22} \text{ W m}^{-2} \text{ Hz}^{-1}$.

3.3. Characteristic Features

Figure 6 shows histograms of the sheath and CIR characteristic parameters. Based on these distributions, statistical medians, means, and standard deviations from the means for all of the sheaths and CIRs are listed in Table 1.

The characteristic parameters exhibit a large range of variation for both sheaths and CIRs. For all sheaths (CIRs), the average V_{sw} varies from ≈ 288 to 761 km s^{-1} (≈ 377 to 719 km s^{-1}) with an average $V_{sw} \approx 443 \text{ km s}^{-1}$ ($\approx 495 \text{ km s}^{-1}$) for all events, the peak N_{sw} varies between ≈ 3.3 and 71.9 cm^{-3} (≈ 2.4 and 81.0 cm^{-3}) with an average $N_{sw} \approx 26.9 \text{ cm}^{-3}$ ($\approx 29.3 \text{ cm}^{-3}$), the peak P_{sw} varies between ≈ 1.0 and 59.9 nPa (≈ 1.4 and 57.2 nPa) with an average $P_{sw} \approx 11.0 \text{ nPa}$ ($\approx 10.5 \text{ nPa}$), the peak T_{sw} varies between $\approx 0.2 \times 10^5$ and $45.6 \times 10^5 \text{ K}$ ($\approx 1.0 \times 10^5$ and $26.4 \times 10^5 \text{ K}$) with an average $T_{sw} \approx 3.7 \times 10^5 \text{ K}$ ($\approx 4.9 \times 10^5 \text{ K}$), the peak B_0 varies from ≈ 2.9 to 43.8 nT (≈ 4.6 to 44.9 nT) with an average $B_0 \approx 13.4 \text{ nT}$ ($\approx 14.8 \text{ nT}$), and the minimum B_z varies from ≈ -39.0 to 0.2 nT (≈ -38.7 to -1.8 nT) with an average $B_z \approx -9.1 \text{ nT}$ ($\approx -10.9 \text{ nT}$) for all events. The duration of sheaths (CIRs) varies between ≈ 1.33 and 33.58 hours (≈ 2.75 and 82.10 hours) with an average duration of ≈ 11.47 hours (≈ 26.47 hours) for all events. The estimated radial extent of the sheaths (CIRs) are ≈ 0.02 to 0.35 AU (≈ 0.03 to 0.98 AU), with an average extent of $\approx 0.12 \text{ AU}$ ($\approx 0.31 \text{ AU}$) for all events. As can be seen from the standard-deviation values (Table 1), the ranges of variation are significantly larger for sheaths than for CIRs.

Wu and Lepping (2016) studied 94 sheaths preceded by interplanetary shocks and followed by MCs using in situ *Wind* measurements in the period 1995–2012. During these sheaths, Kilpua, Koskinen, and Pulkkinen (2017) explored the distributions of solar-wind plasma and IMF parameters measured by the *Advanced Composition Explorer* (ACE) and

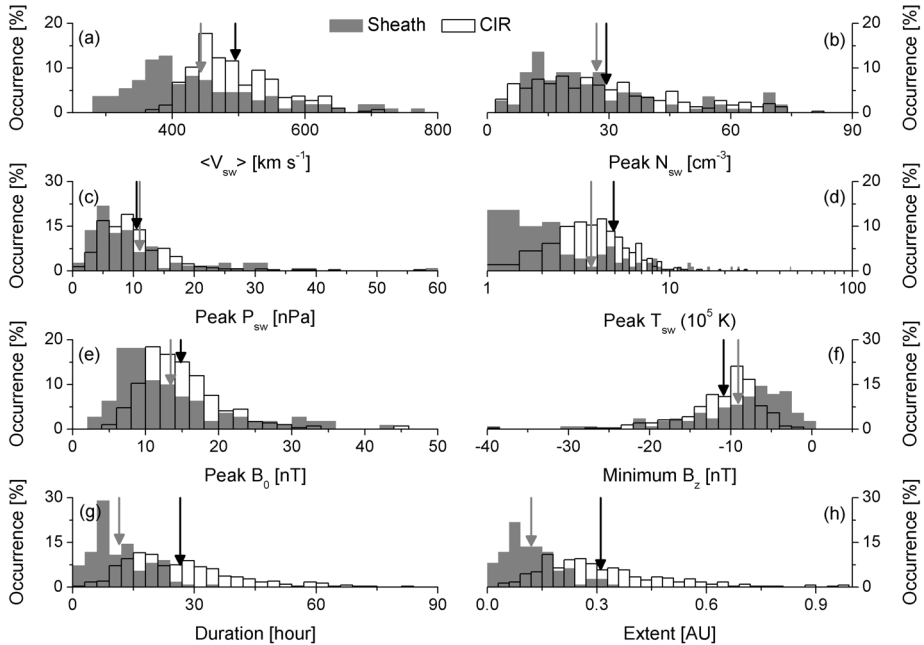


Figure 6 Histograms of (a) average V_{sw} , (b) peak N_{sw} , (c) peak P_{sw} , (d) peak T_{sw} , (e) peak B_0 , (f) minimum B_z during sheaths and CIRs, and (g) duration, and (h) radial extent of sheaths and CIRs. Gray and empty histograms correspond to sheaths and CIRs, respectively. Downward arrows indicate mean values of the parameters for sheaths (gray) and CIRs (black).

Table 1 Statistical characteristics and geomagnetic impacts of sheaths and CIRs.

Parameter	Interplanetary sheath		CIR		p -value
	Median	Mean \pm SD ^a	Median	Mean \pm SD ^a	
V_{sw} [km s ⁻¹]	412	443 \pm 106	480	495 \pm 65	< 0.0001
N_{sw} [cm ⁻³]	22.0	26.9 \pm 17.6	25.7	29.3 \pm 18.0	0.2310
P_{sw} [nPa]	7.7	11.0 \pm 9.6	9.0	10.5 \pm 6.7	0.5566
T_{sw} [10 ⁵ K]	1.76	3.70 \pm 5.76	4.26	4.91 \pm 3.13	0.0074
B_0 [nT]	10.9	13.4 \pm 8.1	13.8	14.8 \pm 5.6	0.0503
B_z [nT]	-7.4	-9.1 \pm 6.8	-9.6	-10.9 \pm 4.7	0.0028
Duration [hours]	9.42	11.47 \pm 6.70	23.58	26.47 \pm 14.09	< 0.0001
Extent [AU]	0.11	0.12 \pm 0.08	0.27	0.31 \pm 0.17	< 0.0001
AE [nT]	724	827 \pm 643	1072	1137 \pm 457	< 0.0001
SYM-H [nT]	-18	-27 \pm 34	-35	-42 \pm 31	< 0.0001

^aStandard deviation.

Wind and time shifted to the Earth's bow-shock nose. Myllys et al. (2016) also developed distributions of solar-wind parameters during geoeffective sheaths. Kilpua et al. (2019) studied 89 sheaths during Solar Cycles 23 and 24. In general, the sheath characteristic solar-wind plasma parameters and IMF values are comparable with those reported in the present work.

Slightly higher plasma speed and stronger southward IMF component reported by Wu and Lepping (2016) could be associated with the fact that the Solar Cycle 24 (present work) is significantly weaker than the previous cycle (see Hajra, 2021c, for a detailed comparison of Solar Cycle 24 with all previous solar cycles in the space age).

The CIR characteristics are comparatively better explored than the sheaths. Alves, Echer, and Gonzalez (2006) studied CIR characteristics using solar-wind measurements shifted to the Earth's bow-shock nose during 1964–2003. Jian et al. (2006) used the ACE and *Wind* measurements to study CIRs during 1995–2004. Jian et al. (2019) explored CIRs encountered by the *Solar Terrestrial Relations Observatory* (STEREO) spacecraft during 2007–2016. The CIR characteristic features obtained by the cited works are found to be more or less consistent with the present results (see Hajra and Sunny, 2022, for a complete discussion on this).

From Figure 6 and Table 1, it is seen that the characteristic solar-wind parameters, duration, and radial extent of the CIRs are higher than those of the sheaths, on average. The statistical significance of this result is verified by the estimated probability factor or the p -value, based on the mean values and standard deviations of each parameter for the sheaths and the CIR events. The p -values are listed in Table 1. A p -value less than 0.05 ($p < 0.05$) indicates that the two means are significantly different (Press et al., 1992). Thus, from the values in the table, we can conclude that sheaths and CIRs are characterized by statistically identical/comparable average N_{sw} , P_{sw} , and IMF B_0 (confirmed by $p > 0.05$), that is, identical plasma and magnetic-field compression amplitudes. However, on average, the CIR has $\approx 12\%$ higher V_{sw} , $\approx 33\%$ higher T_{sw} , $\approx 20\%$ stronger IMF B_z , $\approx 131\%$ longer duration, and $\approx 158\%$ larger radial extent in comparison to the sheath.

3.4. Geoeffectiveness

Geomagnetic activity during each of the sheaths and CIRs is characterized by the maximum AE and the minimum SYM-H values during the events. Distributions of the AE and SYM-H values for all sheaths and CIRs are shown in Figure 7. Their statistical values are summarized in Table 1. AE varies from 21 to 2803 nT (57 to 2698 nT) for sheaths (CIRs) with an average AE of 827 nT (1137 nT) for all sheaths (CIRs). The SYM-H index varies between 21 and -152 nT (1 and -223 nT) with an average of -27 nT (-42 nT) for all sheaths (CIRs). Thus, the average AE activity is $\approx 38\%$ and the SYM-H activity is $\approx 55\%$ stronger during CIRs than during the sheaths.

Table 2 lists the percentage of all sheaths and CIRs causing geomagnetic storms with the minimum SYM-H ≤ -50 nT. While their efficiency in causing an intense storm is more or less the same, CIRs are found to be more efficient in causing moderate storms than sheaths.

The CIR geoeffectiveness reported in this work is consistent with the results reported by Alves, Echer, and Gonzalez (2006) for CIRs during 1964–2003, and by Chi et al. (2018) for CIRs during 1995–2016. From the analysis of all intense geomagnetic storms (with minimum Dst ≤ -100 nT) during Solar Cycle 23, Huttunen and Koskinen (2004) and Echer et al. (2008) concluded that the largest fraction of the intense storms are caused by the sheaths upstream of the MCs. In fact, a significant number of ICME-related storms are suggested to be pure sheath-induced storms (e.g., Tsurutani et al., 1988; Huttunen, Koskinen, and Schwenn, 2002; Huttunen and Koskinen, 2004). However, to our knowledge, the fraction of all the sheaths causing geomagnetic storms and their solar-cycle variation are reported in the present work for the first time.

Stacked histograms in Figure 8 show the percentage of sheaths (Figure 8(a)) and CIRs (Figure 8(b)) causing moderate (empty column) and intense storms (black column) in each year of observation. The $F_{10.7}$ solar flux is shown for a reference to the solar cycle.

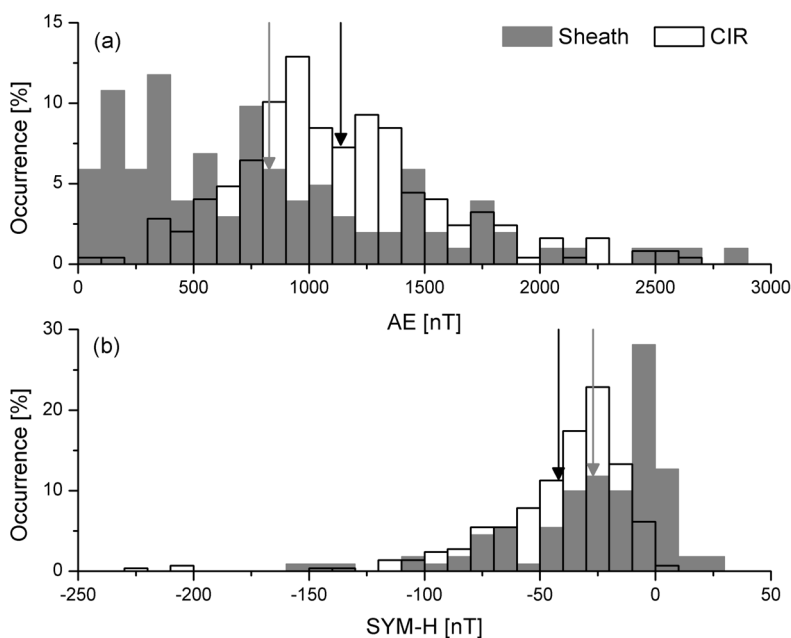


Figure 7 Histograms of (a) AE and (b) SYM-H during sheaths (gray) and CIRs (empty). Downward arrows indicate mean values of AE and SYM-H for sheaths (gray) and CIRs (black).

Table 2 Geoeffectiveness of sheaths and CIRs.

Storm type	Sheath	CIR
Moderate ($-50 \text{ nT} \geq \text{SYM-H} > -100 \text{ nT}$)	14%	25%
Intense ($\text{SYM-H} \leq -100 \text{ nT}$)	4%	5%
All ($\text{SYM-H} \leq -50 \text{ nT}$)	18%	30%

While the sheath occurrence is well organized with the solar-flux variation (Figure 5), their geoeffectiveness seems to be independent of the solar-cycle phase (Figure 8(a)). On the other hand, the CIR geoeffectiveness is prominently correlated to the solar-flux variation, that is, the CIR geoeffectiveness decreases with decreasing solar flux (Figure 8(b)). The latter result was attributed to the enhancement of the CIR geoeffectiveness during the solar maximum owing to the CIR–ICME interaction (e.g., Chi et al., 2018; Hajra and Sunny, 2022, and references therein).

4. Conclusions

Based on a comparative statistical study on 110 interplanetary sheaths and 290 CIRs encountered by the Earth during Solar Cycle 24 (from January 2008 to December 2019), we obtained the following results:

- i) Both sheaths and CIRs represent compressed and turbulent solar-wind plasma and IMF. The turbulence is characterized by enhanced IMF variances (compared to the ambient

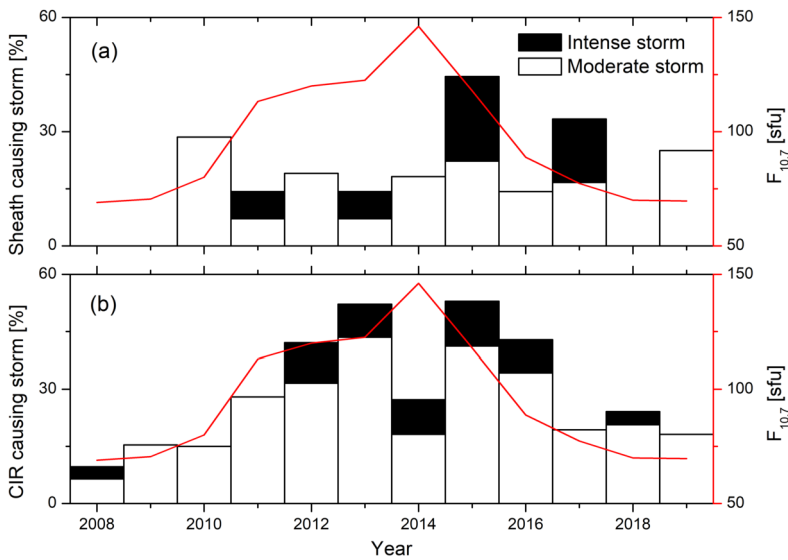


Figure 8 Stacked column chart showing percentage of (a) sheaths and (b) CIRs causing moderate (empty) and intense storms (black).

solar wind), and ≈ 15 -minutes- to 1-hour-scale fluctuations as revealed by wavelet and periodogram analyses.

- ii) While both sheaths and CIRs are compressed plasma regions, their solar-wind plasma and IMF characteristics are significantly different. On average, the CIRs are $\approx 12\%$ faster, $\approx 33\%$ hotter, $\approx 20\%$ stronger in the southward IMF component, $\approx 131\%$ longer in duration, and $\approx 158\%$ wider in radial extent than the sheaths.
- iii) The geomagnetic activity is found to be stronger during the CIRs than the sheaths. The average auroral electrojet index [AE] is $\approx 38\%$ stronger, and the symmetric ring-current index [SYM-H] is $\approx 55\%$ stronger during the CIRs than the sheaths.
- iv) The geoeffectiveness of the CIRs is found to be significantly higher than the sheaths. About 25% of all CIRs and $\approx 14\%$ of all sheaths caused moderate storms ($-50 \text{ nT} \geq \text{SYM-H} > -100 \text{ nT}$). About 5% of all CIRs and $\approx 4\%$ of all sheaths caused intense storms ($\text{SYM-H} \leq -100 \text{ nT}$).

We presented here a comparative study on the occurrences, characteristics, and geoeffectiveness of interplanetary sheaths and CIRs. Both events are characterized by almost identical plasma and magnetic-field compression and turbulence characteristics upstream of the Earth. However, higher geoeffectiveness of the CIRs than the sheaths is reported here for the first time. This is proposed to be caused by enhanced solar-wind–magnetosphere energy coupling efficiency owing to faster, hotter plasma and stronger southward IMFs during the CIRs. A strong IMF southward component is the most important factor for the magnetic reconnection (Dungey, 1961) with the (northward) geomagnetic fields at the Earth’s dayside magnetopause. In addition, significantly longer duration and larger radial extent of the CIRs compared to the sheaths seem to be important contributors for enhanced magnetospheric disturbances during the CIRs. A further study on the solar-wind–magnetosphere coupling processes during the events can be carried out to verify the present results.

Appendix

Table 3 presents a catalog of all interplanetary sheaths identified from January 2008 through December 2019. The approximate start and end times are given as the day of the year. The table is available in the Electronic Supplementary Material.

Table 3 Catalog of all interplanetary sheaths under this study. The approximate start and end times at Earth are given as the day of the year [DOY].

Year	Start [DOY]	End [DOY]
2008	261.05	261.18
2008	338.40	339.54
2008	351.33	352.14
2009	25.94	26.26
2009	34.84	35.12
2009	70.94	71.06
2009	112.46	112.56
2009	154.60	154.88
2009	178.50	178.83
2009	273.06	273.20
2009	305.14	305.43
2009	318.17	318.48
2009	346.24	346.88
2010	1.72	1.97
2010	95.34	95.54
2010	101.50	102.08
2010	148.11	148.88
2010	172.01	172.29
2010	215.74	216.23
2010	303.43	304.08
2011	24.30	24.41
2011	49.07	49.92
2011	88.63	88.94
2011	119.27	119.62
2011	148.05	148.27
2011	155.87	156.12
2011	168.12	168.18
2011	181.60	181.78
2011	260.17	260.59
2011	278.31	278.43
2011	297.78	298.06
2011	305.39	306.04
2011	311.33	312.24
2011	332.91	333.81
2012	22.25	22.51
2012	45.32	45.88
2012	57.91	58.79

Table 3 (Continued)

Year	Start [DOY]	End [DOY]
2012	68.46	68.83
2012	72.39	72.67
2012	75.54	75.78
2012	114.14	114.73
2012	124.09	125.21
2012	136.10	137.50
2012	168.43	168.95
2012	196.72	197.30
2012	225.59	225.83
2012	231.17	231.50
2012	245.03	245.38
2012	248.96	249.29
2012	274.48	274.95
2012	282.12	282.65
2012	286.00	286.80
2012	305.64	306.03
2012	317.98	318.36
2012	328.92	329.53
2013	17.01	17.57
2013	19.72	19.97
2013	76.25	76.60
2013	103.95	104.72
2013	120.41	120.52
2013	157.13	157.65
2013	178.61	179.10
2013	185.73	186.09
2013	193.70	194.24
2013	275.08	275.98
2013	312.90	312.98
2013	334.87	335.17
2013	348.77	349.71
2013	358.92	359.22
2014	36.59	37.14
2014	46.49	47.03
2014	49.30	49.63
2014	95.38	95.94
2014	110.44	111.36
2014	158.70	159.81
2014	180.79	180.90
2014	184.03	184.12
2014	231.28	231.72
2014	238.17	239.13
2014	255.68	255.95
2015	90.36	90.81

Table 3 (Continued)

Year	Start [DOY]	End [DOY]
2015	99.10	99.94
2015	126.08	126.74
2015	130.25	130.55
2015	173.78	174.07
2015	250.58	251.06
2015	297.78	298.58
2015	310.75	311.28
2015	353.69	354.57
2016	18.92	19.46
2016	104.70	105.40
2016	107.24	108.13
2016	201.98	202.51
2016	286.92	287.26
2016	308.77	309.60
2016	314.29	315.05
2017	103.65	104.05
2017	147.66	147.90
2017	197.25	197.99
2017	233.93	234.26
2017	249.99	250.44
2017	250.95	251.10
2018	68.01	68.92
2018	157.49	157.73
2018	191.17	191.53
2018	237.10	237.56
2019	130.74	130.99
2019	133.99	134.35
2019	146.93	147.28
2019	315.26	315.43

Supplementary Information The online version contains supplementary material available at <https://doi.org/10.1007/s11207-022-02020-6>.

Acknowledgments R. Hajra would like to thank Bruce T. Tsurutani for helpful scientific discussions.

Author Contribution R. Hajra planned the work. J.V. Sunny identified the events to study, and did the major part of the analysis. A.G. Nair, M. Babu, and R. Hajra partially contributed to the analysis. R. Hajra prepared the first draft, and helped in interpretation and discussion of the results. All authors contributed to and approved the final version of the paper.

Funding The work of R. Hajra is funded by the Science and Engineering Research Board (SERB, grant no. SB/S2/RJN-080/2018), a statutory body of the Department of Science and Technology (DST), Government of India through the Ramanujan Fellowship.

Data Availability The solar-wind plasma and IMF data are available at NASA's OMNIWeb (omniweb.gsfc.nasa.gov/). The CME information is available at the *Coordinated Data Analysis Workshops*

(CDAW; cdaw.gsfc.nasa.gov/). The coronal hole images are available at the *Solar Dynamics Observatory* (SDO; sdo.gsfc.nasa.gov/). The geomagnetic indices are available at the *World Data Center for Geomagnetism*, Kyoto, Japan (WDC; wdc.kugi.kyoto-u.ac.jp/). The $F_{10.7}$ solar fluxes are available at the *Laboratory for Atmospheric and Space Physics Interactive Solar Irradiance Data Center* (lasp.colorado.edu/lisird/). The CIR event list is obtained from the Electronic Supplementary Material available at DOI.

Declarations

Disclosure of Potential Conflicts of Interest The authors declare that they have no conflicts of interest.

References

- Alves, M.V., Echer, E., Gonzalez, W.D.: 2006, Geoeffectiveness of corotating interaction regions as measured by Dst index. *J. Geophys. Res.* **111**(A7), A07S05. DOI.
- Belcher, J.W., Davis, L. Jr.: 1971, Large-amplitude Alfvén waves in the interplanetary medium, 2. *J. Geophys. Res.* **76**(16), 3534. DOI.
- Burlaga, L.F.: 1974, Interplanetary stream interfaces. *J. Geophys. Res.* **79**(25), 3717. DOI.
- Burlaga, L., Sittler, E., Mariani, F., Schwenn, R.: 1981, Magnetic loop behind an interplanetary shock: Voyager, Helios, and imp 8 observations. *J. Geophys. Res.* **86**, 6673. DOI.
- Cannon, P., Angling, M., Barclay, L., Curry, C., Dyer, C., Edwards, R., Greene, G., Hapgood, M., Horne, R., Jackson, D., Mitchell, C., Owen, J., Richards, A., Rogers, C., Ryden, K., Saunders, S., Sweeting, M., Tanner, R., Thomson, A., Underwood, C.: 2013, Extreme space weather: Impacts on engineered systems and infrastructure. Technical report, Royal Academy of Engineering, Prince Philip House, 3 Carlton House Terrace, London SW1Y 5DG. 1-903496-95-0. www.raeng.org.uk/spaceweather.
- Chi, Y., Shen, C., Luo, B., Wang, Y., Xu, M.: 2018, Geoeffectiveness of stream interaction regions from 1995 to 2016. *Space Weather* **16**, 1960. DOI.
- Davis, J.L.: 1966, Models of the interplanetary fields and plasma flow. In: Mackin, R.J.J., Neugebauer, M. (eds.) *The Solar Wind, Proceedings of a Conference Held 1-4 April, 1964 at the California Institute of Technology*, Pergamon Press, Oxford, 147.
- Davis, J.C.: 2002, *Statistics and Data Analysis in Geology*, Wiley, New York. ISBN 978-0-471-17275-8.
- Davis, J.L., Smith, E.J., Coleman, J.P.J., Sonett, C.P.: 1966, Interplanetary magnetic measurements. In: Mackin, R.J.J., Neugebauer, M. (eds.) *The Solar Wind, Proceedings of a Conference Held 1-4 April, 1964 at the California Institute of Technology*, Pergamon Press, Oxford, 35.
- Dessler, A.J., Parker, E.N.: 1959, Hydromagnetic theory of geomagnetic storms. *J. Geophys. Res.* **64**, 2239. DOI.
- Dungey, J.W.: 1961, Interplanetary magnetic field and the auroral zones. *Phys. Rev. Lett.* **6**, 47. DOI.
- Echer, E., Gonzalez, W.D., Guarnieri, F.L., Dal Lago, A., Vieira, L.E.A.: 2005, Introduction to space weather. *Adv. Space Res.* **35**, 855. DOI.
- Echer, E., Gonzalez, W.D., Tsurutani, B.T., Gonzalez, A.L.C.: 2008, Interplanetary conditions causing intense geomagnetic storms ($Dst \leq -100$ nT) during solar cycle 23 (1996–2006). *J. Geophys. Res.* **113**, A05221. DOI.
- Gardner, L., Sojka, J.J., Schunk, R.W., Heelis, R.: 2012, Changes in thermospheric temperature induced by high-speed solar wind streams. *J. Geophys. Res.* **117**, A12303. DOI.
- Gonzalez, W.D., Joselyn, J.A., Kamide, Y., Kroehl, H.W., Rostoker, G., Tsurutani, B.T., Vasyliunas, V.M.: 1994, What is a geomagnetic storm? *J. Geophys. Res.* **99**, 5771. DOI.
- Gosling, J.T., Hundhausen, A.J., Bame, S.J.: 1976, Solar wind stream evolution at large heliocentric distances: Experimental demonstration and the test of a model. *J. Geophys. Res.* **81**(13), 2111. DOI.
- Gosling, J.T., Asbridge, J.R., Bame, S.J., Feldman, W.C.: 1978, Solar wind stream interfaces. *J. Geophys. Res.* **83**(A4), 1401. DOI.
- Hajra, R.: 2021a, Variation of the interplanetary shocks in the inner heliosphere. *Astrophys. J.* **917**, 91. DOI.
- Hajra, R.: 2021b, Seasonal dependence of the Earth's radiation belt – New insights. *Ann. Geophys.* **39**, 181. DOI.
- Hajra, R.: 2021c, Weakest solar cycle of the Space Age: A study on solar wind–magnetosphere energy coupling and geomagnetic activity. *Solar Phys.* **296**, 33. DOI.
- Hajra, R., Sunny, J.V.: 2022, Corotating interaction regions during solar cycle 24: A study on characteristics and geoeffectiveness. *Solar Phys.* **297**, 30. DOI.
- Hajra, R., Tsurutani, B.T.: 2018, Chapter 14 - magnetospheric “killer” relativistic electron dropouts (REDs) and repopulation: A cyclical process. In: Buzulukova, N. (ed.) *Extreme Events in Geospace*, Elsevier, Amsterdam, 373. ISBN 978-0-12-812700-1. DOI.

- Hajra, R., Tsurutani, B.T.: 2022, Near-Earth sub-Alfvénic solar winds: Interplanetary origins and geomagnetic impacts. *Astrophys. J.* **926**, 135. DOI.
- Hajra, R., Tsurutani, B.T., Lakhina, G.S.: 2020, The complex space weather events of 2017 September. *Astrophys. J.* **899**, 3. DOI.
- Hajra, R., Echer, E., Tsurutani, B.T., Gonzalez, W.D.: 2013, Solar cycle dependence of high-intensity long-duration continuous AE activity (HILDCAA) events, relativistic electron predictors? *J. Geophys. Res.* **118**(9), 5626. DOI.
- Hajra, R., Tsurutani, B.T., Echer, E., Gonzalez, W.D.: 2014, Relativistic electron acceleration during high-intensity, long-duration, continuous AE activity (HILDCAA) events: Solar cycle phase dependences. *Geophys. Res. Lett.* **41**, 1876. DOI.
- Hajra, R., Tsurutani, B.T., Echer, E., Gonzalez, W.D., Brum, C.G.M., Vieira, L.E.A., Santolik, O.: 2015a, Relativistic electron acceleration during HILDCAA events: Are precursor CIR magnetic storms important? *Earth Planets Space* **67**, 109. DOI.
- Hajra, R., Tsurutani, B.T., Echer, E., Gonzalez, W.D., Santolik, O.: 2015b, Relativistic ($e > 0.6$, > 2.0 , and > 4.0 MeV) electron acceleration at geosynchronous orbit during high-intensity, long-duration, continuous AE activity (HILDCAA) events. *Astrophys. J.* **799**, 39. DOI.
- Hajra, R., Tsurutani, B.T., Brum, C.G.M., Echer, E.: 2017, High-speed solar wind stream effects on the topside ionosphere over Arecibo: A case study during solar minimum. *Geophys. Res. Lett.* **44**, 7607. DOI.
- Hajra, R., Marques de Souza Franco, A., Echer, E., José Alves Bolzan, M.: 2021, Long-term variations of the geomagnetic activity: A comparison between the strong and weak solar activity cycles and implications for the space climate. *J. Geophys. Res.* **126**, e2020JA028695. DOI.
- Huttunen, K.E.J., Koskinen, H.E.J.: 2004, Importance of post-shock streams and sheath region as drivers of intense magnetospheric storms and high-latitude activity. *Ann. Geophys.* **22**, 1729. DOI.
- Huttunen, K.E.J., Koskinen, H.E.J., Schwenn, R.: 2002, Variability of magnetospheric storms driven by different solar wind perturbations. *J. Geophys. Res.* **107**, SMP 20. DOI.
- Iyemori, T., Takeda, M., Nose, M., Odagi, Y., Toh, H.: 2010, Mid-latitude geomagnetic indices ASY and SYM for 2009 (provisional). wdc.kugi.kyoto-u.ac.jp/aeasy/asy.pdf.
- Jian, L., Russell, C.T., Luhmann, J.G., Skoug, R.M.: 2006, Properties of stream interactions at one AU during 1995–2004. *Solar Phys.* **239**, 337. DOI.
- Jian, L.K., Luhmann, J.G., Russell, C.T., Galvin, A.B.: 2019, Solar terrestrial relations observatory (STEREO) observations of stream interaction regions in 2007–2016: Relationship with heliospheric current sheets, solar cycle variations, and dual observations. *Solar Phys.* **294**, 31. DOI.
- Kennel, C.F., Edmiston, J.P., Hada, T.: 1985, *A Quarter Century of Collisionless Shock Research*, Am. Geophys. Union, Washington, 1. ISBN 9781118664032. DOI.
- Kilpua, E., Koskinen, H.E.J., Pulkkinen, T.I.: 2017, Coronal mass ejections and their sheath regions in interplanetary space. *Living Rev. Solar Phys.* **14**, 5. DOI.
- Kilpua, E.K.J., Hietala, H., Koskinen, H.E.J., Fontaine, D., Turc, L.: 2013, Magnetic field and dynamic pressure ULF fluctuations in coronal-mass-ejection-driven sheath regions. *Ann. Geophys.* **31**, 1559. DOI.
- Kilpua, E.K.J., Fontaine, D., Moissard, C., Ala-Lahti, M., Palmerio, E., Yordanova, E., Good, S.W., Kalliokoski, M.M.H., Lumme, E., Osmann, A., Palmroth, M., Turc, L.: 2019, Solar wind properties and geospace impact of coronal mass ejection-driven sheath regions: Variation and driver dependence. *Space Weather* **17**, 1257. DOI.
- Klein, L.W., Burlaga, L.F.: 1982, Interplanetary magnetic clouds at 1 AU. *J. Geophys. Res.* **87**, 613. DOI.
- Lakhina, G.S., Hajra, R., Tsurutani, B.T.: 2020, In: Gupta, H.K. (ed.) *Geomagnetically Induced Currents*, Springer, Cham, 1. ISBN 978-3-030-10475-7. DOI.
- Landau, L.D., Lifshitz, E.M.: 1960, *Electrodynamics of Continuous Media*, 2nd edn. Pergamon Press, New York. ISBN 9780080570600.
- Lei, J., Thayer, J.P., Wang, W., McPherron, R.L.: 2011, Impact of CIR storms on thermosphere density variability during the solar minimum of 2008. *Solar Phys.* **274**, 427. DOI.
- Lomb, N.R.: 1976, Least-squares frequency analysis of unequally spaced data. *Astrophys. Space Sci.* **39**, 447. DOI.
- Marques de Souza Franco, A., Hajra, R., Echer, E., Bolzan, M.J.A.: 2021, Seasonal features of geomagnetic activity: A study on the solar activity dependence. *Ann. Geophys.* **39**, 929. DOI.
- Moissard, C., Fontaine, D., Savoini, P.: 2019, A study of fluctuations in magnetic cloud-driven sheaths. *J. Geophys. Res.* **124**, 8208. DOI.
- Myllys, M., Kilpua, E.K.J., Lavraud, B., Pulkkinen, T.I.: 2016, Solar wind-magnetosphere coupling efficiency during ejecta and sheath-driven geomagnetic storms. *J. Geophys. Res.* **121**, 4378. DOI.
- Pizzo, V.J.: 1985, *Interplanetary Shocks on the Large Scale: A Retrospective on the Last Decade's Theoretical Efforts*, Am. Geophys. Union, Washington, 51. ISBN 9781118664179. DOI.

- Press, W.H., Teukolsky, S.A., Vetterling, W.T., Flannery, B.P.: 1992, *Numerical Recipes in C: The Art of Scientific Computing*, 2nd edn. Cambridge University Press, Cambridge. ISBN 0521431085.
- Reiff, P.H.: 1990, The use and misuse of statistics in space physics. *J. Geomagn. Geoelectr.* **42**, 1145. DOI.
- Richardson, I.G., Cane, H.V.: 2012, Solar wind drivers of geomagnetic storms during more than four solar cycles. *J. Space Weather Space Clim.* **2**, A01. DOI.
- Rostoker, G.: 1972, Geomagnetic indices. *Rev. Geophys.* **10**, 935. DOI.
- Scargle, J.D.: 1982, Studies in astronomical time series analysis. II. Statistical aspects of spectral analysis of unevenly spaced data. *Astrophys. J.* **263**, 835. DOI.
- Schwabe, H.: 1844, Sonnen-beobachtungen im jahre 1843. *Astron. Nachr.* **21**, 233.
- Smith, E.J., Wolfe, J.H.: 1976, Observations of interaction regions and corotating shocks between one and five AU: Pioneers 10 and 11. *Geophys. Res. Lett.* **3**(3), 137. DOI.
- Torrence, C., Compo, G.P.: 1998, A practical guide to wavelet analysis. *Bull. Am. Meteorol. Soc.* **79**, 61.
- Tsurutani, B.T., Gonzalez, W.D.: 1987, The cause of high-intensity long-duration continuous AE activity (HILDCAAs): Interplanetary Alfvén wave trains. *Planet. Space Sci.* **35**, 405. DOI.
- Tsurutani, B.T., Gonzalez, W.D.: 1997, *The Interplanetary Causes of Magnetic Storms: A Review*, Am. Geophys. Union, Washington, 77. ISBN 9781118664612. DOI.
- Tsurutani, B.T., Lin, R.P.: 1985, Acceleration of > 47 keV ions and > 2 keV electrons by interplanetary shocks at 1 AU. *J. Geophys. Res.* **90**, 1. DOI.
- Tsurutani, B.T., Smith, E.J., Pyle, K.R., Simpson, J.A.: 1982, Energetic protons accelerated at corotating shocks: Pioneer 10 and 11 observations from 1 to 6 AU. *J. Geophys. Res.* **87**, 7389. DOI.
- Tsurutani, B.T., Gonzalez, W.D., Tang, F., Akasofu, S.I., Smith, E.J.: 1988, Origin of interplanetary southward magnetic fields responsible for major magnetic storms near solar maximum (1978–1979). *J. Geophys. Res.* **93**, 8519. DOI.
- Tsurutani, B.T., Ho, C.M., Arballo, J.K., Goldstein, B.E., Balogh, A.: 1995, Large amplitude IMF fluctuations in corotating interaction regions: Ulysses at midlatitudes. *Geophys. Res. Lett.* **22**, 3397. DOI.
- Tsurutani, B.T., Gonzalez, W.D., Gonzalez, A.L.C., Guarnieri, F.L., Gopalswamy, N., Grande, M., Kamide, Y., Kasahara, Y., Lu, G., Mann, I., McPherron, R., Soraas, F., Vasyliunas, V.: 2006, Corotating solar wind streams and recurrent geomagnetic activity: A review. *J. Geophys. Res.* **111**(A7), A07S01. DOI.
- Tsurutani, B.T., Lakhina, G.S., Verkhoglyadova, O.P., Gonzalez, W.D., Echer, E., Guarnieri, F.L.: 2011, A review of interplanetary discontinuities and their geomagnetic effects. *J. Atmos. Solar-Terr. Phys.* **73**, 5. DOI.
- Tsurutani, B.T., Hajra, R., Echer, E., Gonzalez, W.D., Santolik, O.: 2016a, Predicting magnetospheric relativistic > 1 MeV electrons. *NASA Tech Briefs* **40**, 20. www.techbriefs.com/component/content/article/ntb/tech-briefs/software/24815.
- Tsurutani, B.T., Hajra, R., Tanimori, T., Takada, A., Remya, B., Mannucci, A.J., Lakhina, G.S., Kozyra, J.U., Shiokawa, K., Lee, L.C., Echer, E., Reddy, R.V., Gonzalez, W.D.: 2016b, Heliospheric plasma sheet (HPS) impingement onto the magnetosphere as a cause of relativistic electron dropouts (REDs) via coherent EMIC wave scattering with possible consequences for climate change mechanisms. *J. Geophys. Res.* **121**, 10130. DOI.
- Wanliss, J.A., Showalter, K.M.: 2006, High-resolution global storm index: Dst versus SYM-H. *J. Geophys. Res.* **111**, A02202. DOI.
- Wu, C.-C., Lepping, R.P.: 2016, Relationships among geomagnetic storms, interplanetary shocks, magnetic clouds, and sunspot number during 1995–2012. *Solar Phys.* **291**, 265. DOI.
- Zurbuchen, T.H., Richardson, I.G.: 2006, In-situ solar wind and magnetic field signatures of interplanetary coronal mass ejections. *Space Sci. Rev.* **123**, 31. DOI.